ELSEVIER

Exciton versus free carrier emission: Implications for photoluminescence efficiency and amplified spontaneous emission thresholds in quasi-2D and 3D perovskites

Yang Li [1,2], Isabel Allegro [1], Milian Kaiser [1], Aditya J. Malla [2], Bryce S. Richards [1,2], Uli Lemmer [1,2], Ulrich W. Paetzold [1,2,*], Ian A. Howard [1,2,*]

[1] Institute of Microstructure Technology, Karlsruhe Institute of Technology, Hermann-von-Helmholtz-Platz 1, 76344 Eggenstein-Leopoldshafen, Germany
[2] Light Technology Institute, Karlsruhe Institute of Technology, Engesserstrasse 13, 76131 Karlsruhe, Germany

Among perovskite semiconductors, quasi-two-dimensional (2D) materials are attractive for the pursuit of electrically driven lasing given their excellent performance in light-emitting diodes (LEDs) and their recent success in continuous-wave optically pumped lasing. We investigate the spontaneous photoluminescence emission and amplified spontaneous emission (ASE) of a series of quasi-2D emitters, and their directly analogous 3D materials formed by removing the 2D organic spacer by annealing. Although the PL photoluminescence (PL) (at low optical excitation power) from quasi-2D films with high 2D spacer fractions can be much brighter than that from their 3D counterparts, the ASE thresholds of these quasi-2D materials tend to be higher. This counter-intuitive behavior is investigated through time-resolved photophysical studies, which reveal the emission in the high-spacer-content quasi-2D perovskite can be exclusively excitonic, and the exciton–exciton annihilation of quasi-2D perovskite starts to take over the exciton dynamics at a low exciton density (<10^{16} cm^{-3}). To lower ASE thresholds in quasi-2D materials it is necessary to increase the volume fraction of thick quantum wells, which we achieve by decreasing the spacer content or by utilizing 1-naphthylmethylamine (NMA) linkers. The increase of the volume fraction of thick quantum wells correlates with an increased contribution of free carrier recombination to the emission process of the quasi-2D materials. These results suggest that material development of quasi-2D materials for gain applications should target fast free charge carrier recombination rates by engineering the well thickness and size and not maximum photoluminescence quantum yields under low power excitation.

Keywords: Quasi-2D perovskite; Light-emitting diodes; Amplified spontaneous emission; Exciton–exciton annihilation

Introduction

Quasi-two-dimensional (2D) perovskites are promising optoelectronic materials for display and lighting technologies due to their excellent luminescent properties, color tunability, good stability and ease of solution processing [1–15]. Light-emitting diodes (LEDs) based on quasi-2D emitters have demonstrated external quantum efficiencies (EQE) over 20% for iodide-based perovskites [6], and over 15% for bromide-based perovskites [7]. Meanwhile, quasi-2D perovskite gain materials recently achieved a breakthrough on room-temperature continuous-wave (CW) lasing [15], giving them front-runner status in the quest to realize a perovskite-based electrically driven laser diode [16–18].

Quasi-2D perovskites are comprised of quantum wells (QWs) with high exciton binding energy [19–21]. For example, in a $BA_2(MA)_{n-1}Pb_nI_{3n+1}$ quasi-2D material as the number of lead

* Corresponding authors.
E-mail addresses: Paetzold, U.W. (ulrich.paetzold@kit.edu), Howard, I.A. (ian.howard@kit.edu).

https://doi.org/10.1016/j.mattod.2021.05.002

halide octahedral sheets increase from $n = 1$ to $n = 5$, the exciton binding energy decreases from approximately 400 to 100 meV [19]. Whereas absorption can be dominated by the stronger excitonic and free-carrier absorption in the thinner QWs, fast energy transfer to the widest QWs precedes emission. This results in debate as to whether the emission of quasi-2D perovskites (from these lowest energy QWs) is excitonic or based on free carrier recombination [6,7,22]. We present a set of experiments examining the different photoluminescence (PL) behavior of quasi-2D and 3D materials that demonstrate the PL of our quasi-2D perovskite thin films is purely excitonic for high spacer contents. This contribution of excitonic emission explains the inferior amplified spontaneous emission thresholds of quasi-2D films despite the superior PL in quasi-2D perovskites compared to their 3D counterparts at low excitation power (as well as the 70 meV lower energy of the quasi-2D material's emission compared to its 3D counterpart). At low excitation power, the first-order process of excitonic emission is already fast and efficient. As intensity increases the second-order free carrier recombination responsible for emission in the 3D becomes more efficient, whereas the excitonic emission efficiency in the quasi-2D materials becomes drastically reduced due to exciton–exciton annihilation (EEA). Reducing the 2D spacer concentration increases the large-n QW volume fraction [7], and our results suggest that increasing the volume fraction of large QWs in the quasi-2D material is critical for reducing the ASE threshold. This agrees with previous literature finding lower ASE thresholds for higher-n QWs [9,10,12], although some previous literature also reports an increase in threshold for higher-n QWs [23]. We find that as the 2D spacer content is reduced, the recombination shifts towards free-carrier recombination, and the ASE threshold is reduced until rougher surfaces at lower 2D spacer contents compromise ASE performance. Interestingly, the decrease in the ASE threshold and participation of free-carrier recombination correlate with the disappearance absorption features of small-n QWs, and reduction in the blue-shift of the emission peak from that of the 3D counterpart.

As mentioned above, solution-processed thin films of quasi-2D perovskites are comprised of QWs with varying thicknesses. As a consequence, these thin films exhibit an energy cascade landscape [3,4] that strongly impacts their emission characteristics. The utilization of quasi-2D materials for stimulated emission was established by Zhang and coworkers in 2018, wherein the concentration of excited states into higher n QWs was suggested to help achieve population inversion [9]. However, the spatial concentration of excitons into the low bandgap QWs also favors higher-order nonradiative processes (i.e., EEA [24–27]), which is likely detrimental to the amplified spontaneous emission (ASE) threshold, and lasing performance. Indeed, in their recent seminal work demonstrating room-temperature continuous-wave lasing in quasi-2D materials, Qin et al. [15] proposed singlet–triplet exciton annihilation (STA) to be a critical mechanism causing lasing death in quasi-2D perovskites. A deeper understanding of the emission mechanism, and potentially exciton dynamics in quasi-2D perovskites is therefore highly desirable from a fundamental and practical standpoint.

As a brief aside considering the potential role of triplet and singlet exciton populations, we note that the EQEs above 15% of LEDs made from the same quasi-2D material as used by Qin and coworkers, translate into internal PL quantum yields (iPLQY) values close to unity [6,7]. This implies that triplet excitons in quasi-2D perovskites can efficiently return to the singlet state by reverse intersystem crossing [28], aided by the presumably negligible splitting of the singlet and triplet energy levels in these materials. Thus, one might expect an equilibrium between singlet and triplet states is formed, and the triplet and singlet exciton populations decay at the same rate. In this case, the decay rate for both exciton states should is dependent on the ratio of the singlet-to-triplet population in equilibrium and the rates of all the recombination channels (including second-order channels such as annihilation). In this context, the transient PL dynamics we focus on elucidating in this work would reveal the annihilation dynamics of the total (singlet plus triplet) exciton population. It will be of ongoing interest to gain a more nuanced understanding of transient populations in singlet and triplet manifolds.

In this paper, quasi-2D perovskite thin films were formed in the standard fashion by adding a large cation, *n*-butylammonium bromide (BABr), 2-phenylethylammonium bromide (PEABr) or 1-naphthylmethylamine bromide (NMABr), to the precursor material of $CsPbBr_3$ (see film processing details in experimental section). We demonstrate that by high temperature annealing these quasi-2D films, 3D films are created (whose X-ray diffraction signature, absorption and emission spectra are identical to those of the neat $CsPbBr_3$ 3D film, see Fig. S1). We note that the 3D films fabricated through high-temperature annealing (HTA) of a quasi-2D film exhibited a significantly different crystal orientation (Fig. S1) and likely morphology compared to the pristine $CsPbBr_3$ 3D film, given the differences in processing routine. The emission characteristics of the quasi-2D perovskite films are compared to the directly analogous 3D perovskite counterparts prepared by the annealing-based conversion of the quasi-2D films. Compared to a 3D film made from neat $CsPbBr_3$, the 3D films created via conversion of a quasi-2D film are much smoother and show significantly lower ASE thresholds. At low optical excitation intensities, the quasi-2D films with high 2D spacer concentration exhibit much brighter emission, but their ASE thresholds are higher than the 3D counterparts. A detailed investigation of the photophysics of the quasi-2D material and the 3D analog reveals conclusively that the emission mechanism in the high-spacer-content quasi-2D material is purely excitonic (and hence first order), while that in the 3D material is based on free carrier recombination (and hence second order). This fully explains why the emission efficiency of the quasi-2D material is much higher at low excited-state densities, but that the first order emission becomes less efficient as second-order EEA turns on. The limited volume fraction of the largest QWs in the quasi-2D structure into which all excited states are concentrated leads to high rates of EEA. On the other hand, the second-order charge carrier recombination that causes emission in the 3D material becomes more efficient as the excited-state density increases, allowing the ASE threshold to be lower in the 3D material.

We demonstrate that the alteration of the 2D spacer content or nature offers control over the volume fraction of low-n QWs, [7] and thereby can tune the recombination mechanism

toward free-charge carrier recombination, which in turn lowers the ASE threshold of the quasi-2D films. Although small concentrations of quasi-2D linkers frustrate the formation of very smooth quasi-2D films, hampering ASE performance through a reduction in the photon density in the film due to increased scattering, we demonstrate that good ASE performance from a quasi-2D material can be obtained by preparing quasi-2D films with low concentrations of NMA spacers, whose emission is dominated by free carrier recombination, then improving the roughness through low-temperature imprinting.

Results

Spontaneous and amplified spontaneous emission

Our investigation on quasi-2D perovskite starts with the role of the BABr spacer. Quasi-2D perovskite films were prepared by spin-coating a precursor solution of a given ratio between $CsPbBr_3$ and BABr, followed by annealing the film at 70 °C. To transform the quasi-2D perovskite into the 3D material (if desired) a further high-temperature annealing (HTA) of the quasi-2D films at 150 °C for 10 min was undertaken. Fig. 1a illustrates the workflow for preparation of quasi-2D and 3D films. The multiple QW (MQW) characteristics of the quasi-2D perovskites are confirmed by the multiple exciton peaks (Fig. 1b shows exemplary data for $CsPbBr_3(BABr)_{0.8}$, whereas data for all samples is shown in Fig. S2). Pronounced peaks originate from the single- (402 nm), double- (434 nm) and triple-layer (462 nm) perovskite QWs [29], and the absorption peak near the band edge comes from the thick QWs (<*n* >). However, as the amount of added BABr decreases, the volume fraction (and hence absorption) of these thin QWs decreases (Fig. S2). The formation of 3D thin films after HTA process is verified through the absence of multiple exciton absorption peaks of low-n QWs ($n = 1–3$). Meanwhile, no additional bleach peak between <*n*> (from quasi-2D sample) and the 3D bleaching band is apparent in the fs-TA spectra of the HTA-3D sample for all the time delays (0–2 ns), and the position and width of the 3D bleaching band do not change with time delay. Hence, absence of QWs signature (both $n = 1–3$ and <*n*>) in the 3D sample indicates the quasi-2D perovskite transforms to the 3D perovskite after the HTA process.

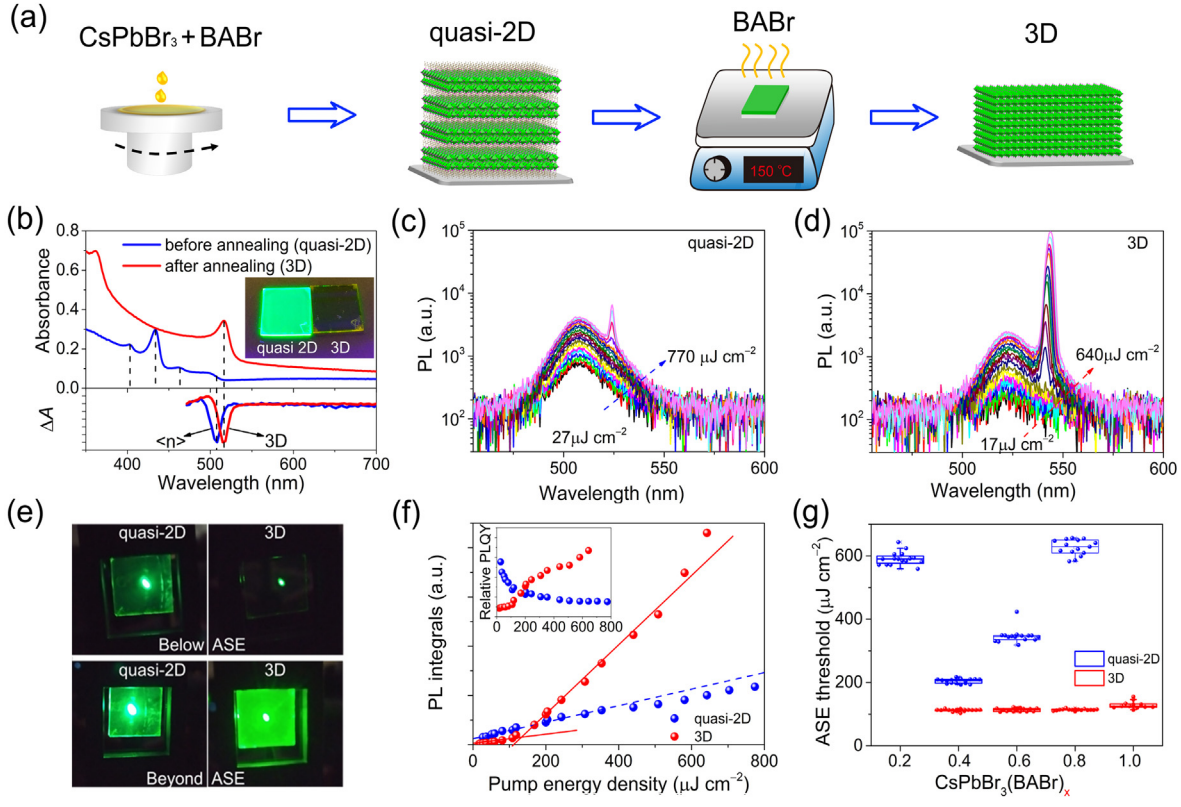

FIGURE 1

PL and ASE characteristics of quasi-2D and 3D perovskite. (a) Schematic diagram of the annealing process to transform quasi-2D into a 3D film. (b) Steady-state (top) and normalized transient (bottom, at 2 ns time delay, excitation: 405 nm and 4 μJ cm^{-2}) ultraviolet–visible (UV–Vis) absorption spectra of films prepared based on the elemental composition of $CsPbBr_3(BABr)_{0.8}$ before and after HTA process, and the dashed lines indicate the exciton peaks located at 402 nm (single layer), 434 nm (double layer) and 462 nm (triple layer), respectively. The inset shows the photograph of the corresponding films under UV light. (c, d) PL spectra of quasi-2D and 3D films following the excitation at 355 nm (1 kHz, 1 ns) under a series of pump energy densities. (e) Photographs of the quasi-2D and 3D films irradiated under a pulse laser beam at the same power (top: below ASE threshold, bottom: beyond ASE threshold). (f) Light-in light-out curves of quasi-2D and 3D films, and the emission outputs were obtained from the integration of the PL spectra in (c, d). The solid/dashed lines are the linear fits for different regimes (the nonlinear scatter data at high power density was neglected for fitting). Inset shows the relative PLQY calculated by dividing the light-out by light-in. (g) ASE threshold statistics of quasi-2D and the corresponding 3D films, and no ASE could be observed from the 3D films made from the elemental composition of $CsPbBr_3(BABr)_{0.2}$.

Varying the annealing temperatures from 70 °C to 250 °C (Fig. S3) reveals the complete removal of the multiple exciton peaks of quasi-2D films at 150 °C. Hence, unless otherwise stated, all the HTA process were conducted at 150 °C in a nitrogen-filled glovebox and all the 3D films discussed in the main text were obtained from HTA process. We cannot rule out the existence of a small amount of 2D spacers in the films after HTA process, but we note that optical properties of the HTA-films are dominated by the 3D $CsPbBr_3$ perovskite, as also revealed in detail below.

Fig. 1c and d show the emission spectra (355 nm excitation, 1 ns pulse length) under varying fluences for the $CsPbBr_3(BABr)_{0.8}$ quasi-2D and 3D films. The data were carefully collected with exactly the same excitation/collection geometry, allowing the absolute PL intensities to be compared. At low excitation fluence (<100 μJ cm^{-2}), the PL intensity of the quasi-2D film is much stronger than for the 3D film. The emission from the quasi-2D film also shows a 70 meV peak shift to higher energy relative to that of the 3D film, consistent with excitonic emission from a QW in the quasi-2D perovskite. The superior brightness of the quasi-2D films under low power excitation is strikingly evident by eye (see Fig. 1b and e, and Figs S2, S3). However, as the fluence increases, the PL intensity of the 3D film becomes similar to, then exceeds that of the quasi-2D film. Furthermore, as shown in Fig. 1c and 1d, the 3D films show an ASE signature at lower fluence (120 μJ cm^{-2}), which remains more pronounced even at the highest fluence.

To estimate the ASE thresholds for $CsPbBr_3(BABr)_{0.8}$ quasi-2D and 3D films, the PL spectra were integrated to compute the emission outputs (light-out), which are shown as the function of excitation power densities (light-in) in Fig. 1f. The light-in light-out curve suggests an ASE threshold of 130 μJ cm^{-2} for the 3D film. In contrast, the quasi-2D film exhibits sublinear light-in light-out characteristics, and no inflection point for ASE threshold is apparent. For this reason, the ASE threshold for the quasi-2D material is estimated as the pump intensity at which the spectral feature of ASE first becomes observable and is established as ~600 μJ cm^{-2}. As depicted in the inset of Fig. 1f, the relative emission efficiencies (derived from the ratio of integrated light-out to light-in) of the $CsPbBr_3(BABr)_{0.8}$ quasi-2D and 3D perovskite films reveal that quasi-2D film exhibits lower emission efficiency with increasing pump energy density. However, the emission efficiency of the 3D film has the opposite trend as compared to the quasi-2D sample, and the relative PLQY increases with increasing excitation fluence. We note that the increase of the estimated relative PLQY beyond the ASE threshold for the 3D films could be influenced by a change in the angular emission pattern, in addition to the higher fraction of radiative recombination at higher charge carrier densities. Meanwhile, the absolute PLQYs (Fig. S4) using an integrating sphere are provided, showing a similar trend compared to the previously discussed relative PLQY. The maximum absolute PLQY of 25% for the $CsPbBr_3(BABr)_{0.8}$ film underlines the good quality of our quasi-2D films [7,30,31]

To minimize the influence of pump pulse duration on ASE threshold and output characteristics [32–34], ASE measurements were also conducted using a 260-fs laser excitation (see Fig. S5). The ASE thresholds decreased one order of magnitude to 12 μJ cm^{-2} for the 3D film, and 20 μJ cm^{-2} for the quasi-2D film. However, the sublinear output behavior of quasi-2D films still existed. We attribute the increase of the ASE threshold with longer pump pulse duration to the reduction of instantaneous excited state and photon densities (see Fig. S6 for details).

The trend of emission (PL) intensity and ASE thresholds were examined for the range of quasi-2D films with different BABr contents and their corresponding 3D counterparts as shown in Fig. 1g. Compared to the quasi-2D films, all the 3D counterparts show inferior emission under low excitation power (see Fig. S2) but achieve lower ASE thresholds (Figs. 1g and S7). Among all the quasi-2D samples, thin films made from the composition of $CsPbBr_3(BABr)_{0.4}$ show the lowest ASE thresholds. As discussed below, we conclude that the higher fractions of large QWs in the quasi-2D materials with lower amounts of the 2D spacer will lead to less fast EEA. A single outlier did not follow this trend in ASE threshold; the quasi-2D film $CsPbBr_3(BABr)_{0.2}$ showed a higher ASE threshold, and the 3D thin films obtained from the elemental composition of $CsPbBr_3(BABr)_{0.2}$ didn't show ASE. This was attributed to the significant scattering loss [35–37] given the larger surface root mean square (RMS) roughness of 30 nm (Fig. S8) of films fabricated from this composition. Work is ongoing to improve the film quality from these low 2D spacer content films.

One additional key result from our work in the context of ASE threshold and surface morphology is highlighted. As shown in Fig. S9, the 3D films directly made from $CsPbBr_3$ (without 2D spacer, hereafter referred to as direct-3D) precursor solution are much rougher than the 3D films made by the annealing of the quasi-2D films. In fact, due to this large roughness (11.6 nm), no ASE could be observed from the former. The process of forming a quasi-2D film then transforming it into the 3D material by HTA yields much better film morphologies and consequently much better ASE thresholds. This result represents an important material fabrication conclusion in its own right.

We note that the PL peak of the quasi-2D materials with all the different concentrations of 2D spacers ($CsPbBr_3(BABr)_{0.2\text{-}1.0}$) stayed almost constant at ~510 nm (slightly blue shift from 516 nm to 505 nm, Fig. S7 and Table S1). This indicates that despite the changing volume fraction of QWs of different sizes, the emission comes from the similar large-n QWs (QW thickness slightly varies) in all cases. The PL of the 3D materials peaks at 525 nm. The blue-shift in the emission from the 3D to the quasi-2D material corresponds to an exciton binding energy of 70 meV. We also note that the ASE shifts to the blue for the quasi-2D materials with larger fractions of the 2D spacer (i.e., the ASE peak shifts closer to the peak of the spontaneous emission). This shift of the ASE peak is consistent with greater long-wavelength reabsorption in the samples with lower 2D spacer content, which would be caused by the greater volume fraction of high-n QWs therein.

To investigate the role of the 2D spacer, 2D films based on $CsPbBr_3$ and PEABr or NMABr were prepared (with varying amounts of the 2D spacer). Also, 3D counterparts were made by transforming these films using the established HTA process. Again, all of these materials show the same trend as described above with the BABr spacer. The PL of the quasi-2D films made from PEABr and NMABr spacers are brighter at low excitation powers but nonetheless exhibit higher ASE thresholds compared

RESEARCH: Original Research

to their 3D counterparts (Fig. S10). This observation reveals that the excellent luminous characteristics of the quasi-2D perovskites at low excitation power densities does generally not translate into lower ASE thresholds. Rather, the 3D materials that are much less bright under low excitation power densities always have significantly lower ASE thresholds.

Excitonic and free carrier emission

To explore the origin of the surprising anti-correlation between the PL and ASE properties, the radiative recombination processes of the $CsPbBr_3(BABr)_{0.8}$ quasi-2D and 3D perovskites are analyzed. As shown in Fig. S4b, we first investigate the dependence between PL integrals and pump power density. Under CW excitation, the slope (under log–log scale) is 0.9 and 1.16 for quasi-2D and 3D indicating the different radiative properties (see Supplementary Note 1). Time-resolved PL (TRPL) under a series of excitation energy densities were then collected with a streak camera upon the excitation by a 344 nm laser with 260 fs pulse length. The PL intensity at time zero, PL_0, was determined by taking the peak intensity of the measured TRPL data. This is shown in Fig. 2a. PL_0 represents the radiative recombination rate at time zero after photoexcitation, at which time the excited-state density can be approximated by the absorbed photon density [38]. Hence, the dependence of PL_0 on the excitation fluence reflects the radiative recombination channel (see Supplementary Note 2). We note that a faster instrumental time resolution can increase the accuracy of the evaluation for the radiative channel (see Fig. S11). A linear increase in PL_0 with excitation fluence indicates that the emission rate scales linearly with the excited-state density, consistent with emission from an excitonic state. This is precisely what is observed for the quasi-2D perovskite: PL_0 linearly increases with fluence, indicating that first order excitonic emission dominates in the quasi-2D perovskite up to the ASE threshold. This shows that the excited-state dynamics are dominated by excitons in the quasi-2D material and can be described as the following differential rate equation [24].

$$-\frac{dn_x}{dt} = k_{ex}n_x + k_{bx}n_x^2 \quad (1)$$

where n_x is the exciton density, t is the time, k_{ex} and k_{bx} are the excitonic emission and EEA rate coefficients, respectively. Based on this model, the TRPL can be further expressed as

$$PL(t) \sim \left(\frac{dn_x}{dt}\right)_{h\nu} = k_{ex}n_x(t) \quad (2)$$

Through numerical integration of the rate equation (Eqn. (1)), we obtain the numerical expression of TRPL based on Eqn. (2), which is globally fitted to the measured TRPL (Fig. 2b). The global fitting generated the coefficients k_{ex} of $2.25*10^7$ s^{-1} and k_{bx} of $2.39*10^{-9}$ cm^3 s^{-1}. QWs with different thickness coexist in the quasi-2D thin films, but given the fast energy funneling (supported by the fast increase in bleaching signal of <*n*> and time-invariant emission spectra, see Figs. S12 and S13), the excited-

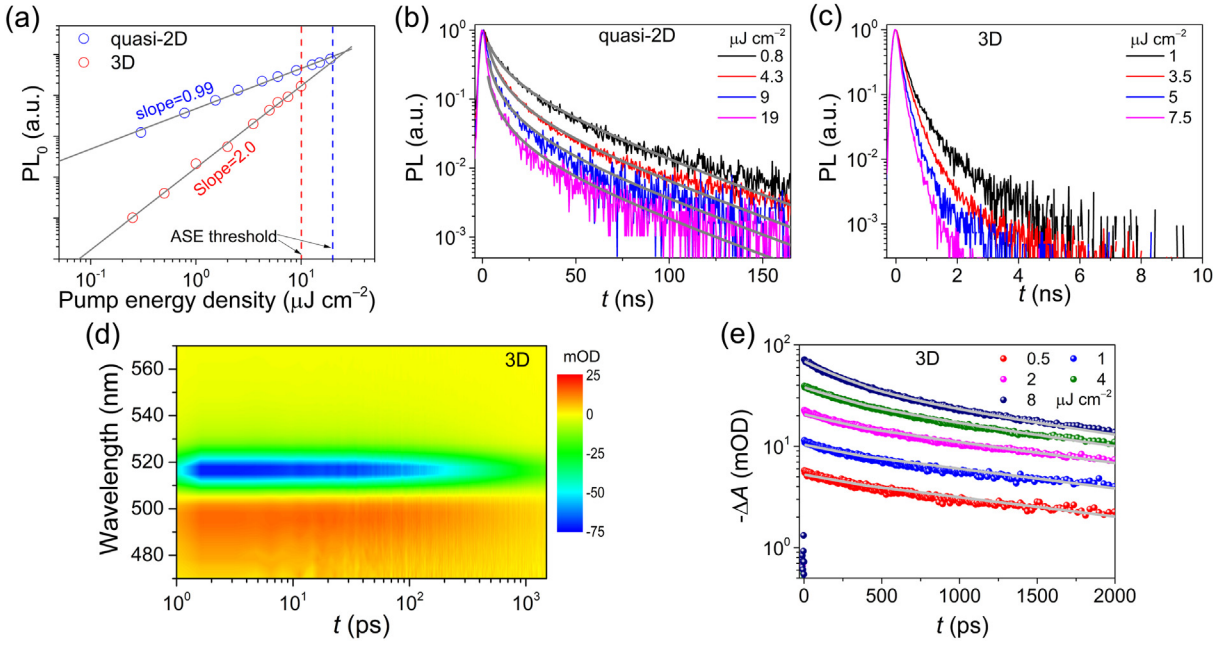

FIGURE 2

Excitonic emission in $CsPbBr_3(BABr)_{0.8}$ quasi-2D perovskite and radiative free charge carrier recombination in 3D perovskite made by HTA of the former film. (a) Plots of PL_0 versus the excitation energy densities. The gray solid lines are the linear fits on the log–log scale indicating that the maximum instantaneous emission scales linearly with the fluence for the quasi-2D material (excitonic emission implies slope = 1), and with the square of the fluence for the 3D material (free carrier emission implies slope = 2). The dashed lines indicate the ASE threshold of quasi-2D (blue) and 3D (red) film. (b, c) Representative normalized TRPL decays of (b) quasi-2D and (c) 3D thin film recorded with a streak camera setup following the excitation at 343 nm (1 kHz, 260 fs). The gray solid lines are the fittings according to the rate equation model described in the text. (d) TA spectra of 3D thin film acquired under 405 nm (260 fs, 1 kHz) laser excitation at the pump energy density of 8 μJ cm^{-2}. (e) Transient absorption traces determined for a series of pump energy densities at the bleaching peak. The gray solid lines indicate fits according to the rate equation model. All measurements were conducted under vacuum and below ASE thresholds.

states will be concentrated into the volume occupied by the thickest QWs. To determine the exciton density in this case, we take the whole volume of the film, as we cannot yet accurately determine the volume fraction occupied by the thickest wells (and therefore the true excited-state density). This will lead k_{bx} to be overestimated. To get the true value of k_{bx} our quoted value should be multiplied by the volume fraction of the film occupied by the largest QWs (see Supplementary Note 3), which is at this time not readily accessible.

If free carrier recombination dominates the emission, the initial emission rate, PL_0, should scale with the square of the excitation fluence. Indeed, this is precisely what is observed for the 3D film (Fig. 2a). For 3D perovskites, the dynamics of free charge carriers after pulsed excitation are determined by the following rate equation [39].

$$-\frac{dn}{dt} = k_1 n + k_2 n^2 + k_3 n^3 \quad (3)$$

where n is the free charge carrier density, k_1, k_2 and k_3 are the trap-assisted, bimolecular and Auger recombination rate coefficients, respectively. As shown in Fig. 2c, the short PL lifetime (<10 ns, first order) indicates a fast trap-assisted recombination process, which accounts for the poor PL efficiency under low excitation power.

We conducted femtosecond transient absorption (fs-TA) measurements to investigate the second and third-order excited-state dynamics in early time range right after photoexcitation with varying fluences. Fig. 2d depicts the TA spectra of 3D film acquired under 405 nm (260 fs, 1 kHz) laser excitation at the pump energy density of 8 μJ cm^{-2}. A prominent bleach near the bandgap is observed, and the corresponding kinetic trace represents the population density decay of charge carriers. TA spectra under a series of pump fluences were acquired, and the corresponding bleaching kinetic traces were shown in Fig. 2e. Through numerically solving of Eqn. (3), the time profile of the charge carrier density under a series of pump energy densities could be obtained, which was further globally fitted to all the bleaching kinetic traces. All the rate coefficients were set free for the global fitting, and the fitted rate coefficients were tabulated in Table 1, which are comparable to the rate coefficients reported in the literature (Table S2). We note that all the fluences were kept below the ASE threshold, to eliminate the influence of ASE on the observed dynamics.

From the linearity of PL_0 data shown in Fig. 2a, and the shape of the PL transients shown in Fig. 2b we can confidently conclude that the excited states in the $CsPbBr_3(BABr)_{0.8}$ quasi-2D material are excitons. The alternative hypothesis, that emission is due to free carrier recombination, with the carrier concentration being affected also by 3rd Auger process is neither consistent with the linearity of PL_0 with fluence, nor with the dynamics that show a varying initial decay rate (increasing with fluence), followed by the same exponential decay at later times irrespective of the fluence.

Analysis of excited-state recombination channels

As shown in Fig. 3a and b, we calculated the carrier density-dependent decay rates for all the recombination channels based on the fitted rate coefficients. The radiative efficiencies were also computed through the ratios of radiative rates to the total decay rates (assuming no monomolecular loss for the excitonic emission). For quasi-2D perovskites, the first order excitonic emission dominates at low exciton density generating the high radiative efficiency, and the lower the exciton density, the higher the radiative efficiency. This consideration could well explain the excellent PL of quasi-2D perovskite at low excitation power. However, the second-order nonradiative process of EEA starts to take over at the exciton density of 10^{16} cm^{-3} (~0.03 μJ cm^{-2}), which is far below the most reported ASE thresholds for quasi-2D perovskites (usually larger than 1 μJ cm^{-2}) [9–15,40–43]. To increase the photon density sufficiently to achieve ASE in this low radiative efficiency regime, a much higher excitation fluence is necessary. This explains the high ASE thresholds of the quasi-2D materials.

In contrast, the ASE threshold of 3D perovskites is located exactly at the regime, where the radiative channel (second order) dominates the free charge carrier recombination (where Auger recombination is not yet dominating). The high radiative efficiency in this regime benefits for a lower ASE threshold of 3D perovskites. Also, the poor PL properties of 3D perovskites at low excitation power could be explained as the low radiative efficiency originated from the trap-assisted charge carrier recombination. Nevertheless, the trap-filling effect [44] and the significantly enhanced free carrier recombination rate under high excitation power weaken the effect of traps on the ASE threshold.

Based on the above in-depth experimental results on exciton dynamics in $CsPbBr_3(BABr)_{0.8}$ quasi-2D perovskite, the exciton decay pathways are schematically illustrated in Fig. 3c. After the excitation, the photo-generated excitons in the quasi-2D thin film quickly funnel to, and emit from thick QW domains. Under low excitation power, excitonic emission can lead to a high PLQY for the quasi-2D perovskite. With increasing excitation power, the increased exciton density in the thick QW domains leads to an increased possibility for exciton–exciton interactions, resulting in the increased EEA. The EEA significantly reduces the emission efficiency as the excitation intensity is increased. Since the PL efficiency becomes low at high excitation fluences, a much higher excitation power is needed to reach the photon density necessary for ASE.

TABLE 1

Rate coefficients obtained from global fitting the TRPL decays of quasi-2D thin film and fs-TA dynamics of 3D thin film.

	k_{ex} or k_1 (s^{-1})	k_{bx} or k_2 (cm^3 s^{-1})	k_3 (cm^6 s^{-1})
quasi-2D	$(2.25 \pm 0.91) \times 10^7$	$(2.39 \pm 0.17) \times 10^{-9}$	–
3D	$(5.59 \pm 0.01) \times 10^8$	$(1.03 \pm 0.08) \times 10^{-9}$	$(0.63 \pm 0.11) \times 10^{-29}$

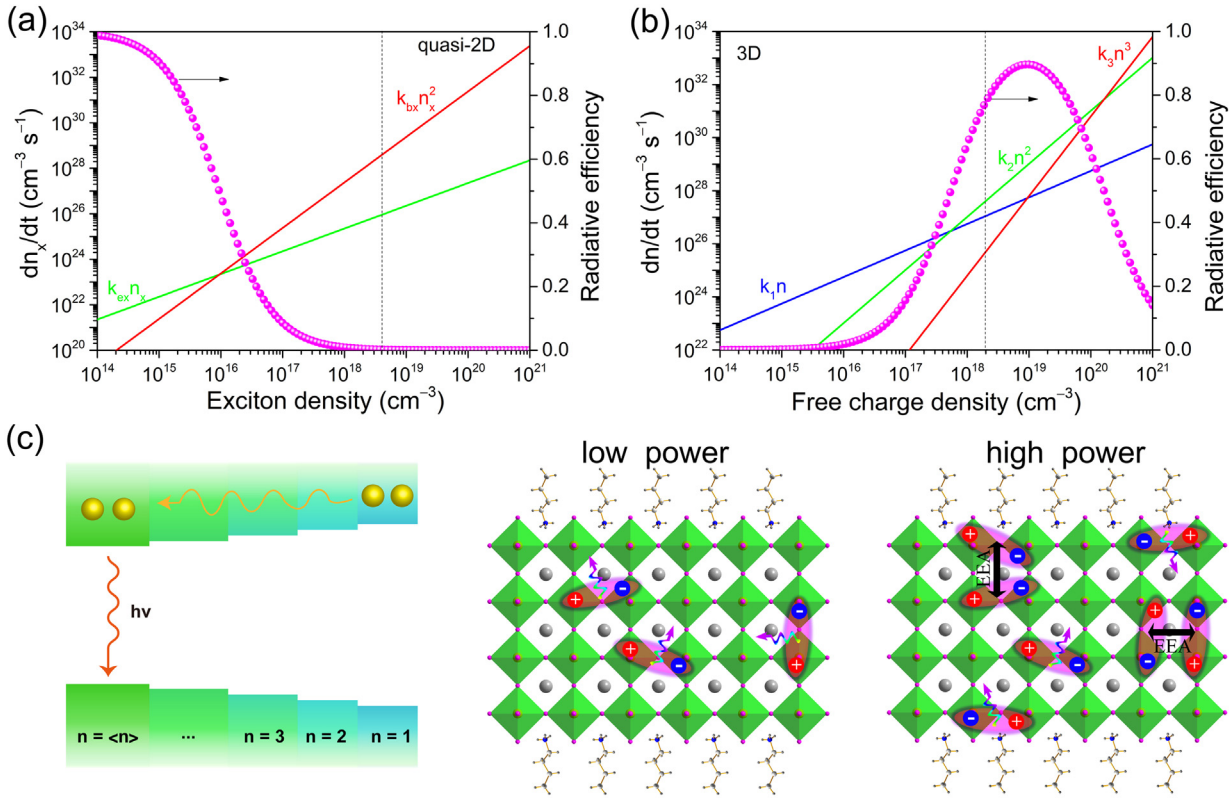

FIGURE 3

Calculated decay rates and radiative efficiencies. Dependence of the exciton/charge carrier density with the decay rates and radiative efficiencies of (a) quasi-2D and (b) 3D thin film. The dashed line is the indication of the ASE threshold for the corresponding perovskites. (c) Schematic illustration of the cascade energy landscape, excitonic emission and EEA process in quasi-2D perovskite.

Optimizing ASE in quasi-2D films

To highlight key findings of this study on how the ASE threshold of quasi-2D films correlates with film roughness and volume fraction of thin QWs, we discuss key parameters affecting the ASE threshold as a function of the 2D spacer concentrations (see Fig. 4). The volume fraction of thin QWs is estimated by taking the ratio of the absorbance of the $n = 2$ QWs (434 nm peak) with the absorbance of the thick (<n>) QWs at 500 nm. Fig. 4 presents this data for BA and NMA ligands. To assess the dominant recombination mechanism for each 2D spacer concentration, the slope of PL_0 (the metric introduced for the $BA_{0.8}$ material in Fig. 2a) is determined for each 2D spacer concentration. Experimental details of the AFM measurements used to determine roughness and the streak camera data sequences to determine the slope of PL_0 are presented in in Figs. S14–S22. For comparison, a similar study on PEA ligands is presented in Fig. S23.

With decreasing concentration of the 2D spacer, the volume fraction of thin QWs steadily decreases (see $A_{n=2}/A_{n=<n>}$) and the roughness of the quasi-2D film is found to increase. While an increase film roughness hampers ASE, as the photon density within the ASE band in the film is reduced by light scattering-induced outcoupling of emitted photons (see detailed discussion from supplementary note 4), the decrease in volume fraction of the low-n QWs favors free charge carrier recombination and, in turn, ASE. This key finding that the lowest threshold is reached when the product of the roughness and the volume fraction of thin QWs is general, considering the consistent trend present for all ligands investigated in this work (NMA, BA, PEA; see Fig. 4 and Fig. S23). Our data show that it is not merely the film roughness that needs to be considered, but that reducing the volume fraction of low-n, thin, QWs is also essential.

We note that the missing ASE threshold data of $BAA_{1.0}$, $PEA_{0.2}$, $PEA_{0.8}$, $PEA_{1.0}$ and $NMA_{0.2}$, $NMA_{0.4}$ is due to the absence of ASE for these samples. For $PEA_{0.2}$, $NMA_{0.2}$ and $NMA_{0.4}$, the absence of ASE is due to the high surface roughness (worse than 5 nm, see Figs. S17 and S20). For $BAA_{1.0}$, $PEA_{0.8}$ and $PEA_{1.0}$, the absence of ASE can be attributed to the high exciton–exciton annihilation loss (see Figs. 4a, S22 and S23).

One important comparison between the BA data and the NMA data (Fig. 4a and 4b) is that the volume fraction of small QWs is always much smaller for the NMA ligand, even when it is present at high concentrations. This leads to significantly lower ASE thresholds for the NMA at high concentrations (0.8 and 1.0) than for the BA ligand at these high concentrations.

To understand this correlation in more detail, we consider how the slope of PL_0 and the PL peak position (sub-ASE threshold) change as a function of ligand and its concentration. For the slope of PL_0 against excitation fluence on a log–log plot. We recall that a value of 2 (a quadratic dependence) indicates free carrier recombination, whereas a slope of 1 (linear dependence) indicates excitonic emission. Similarly, the PL peak position for pure free carrier emission in the 3D samples is at 2.36 eV,

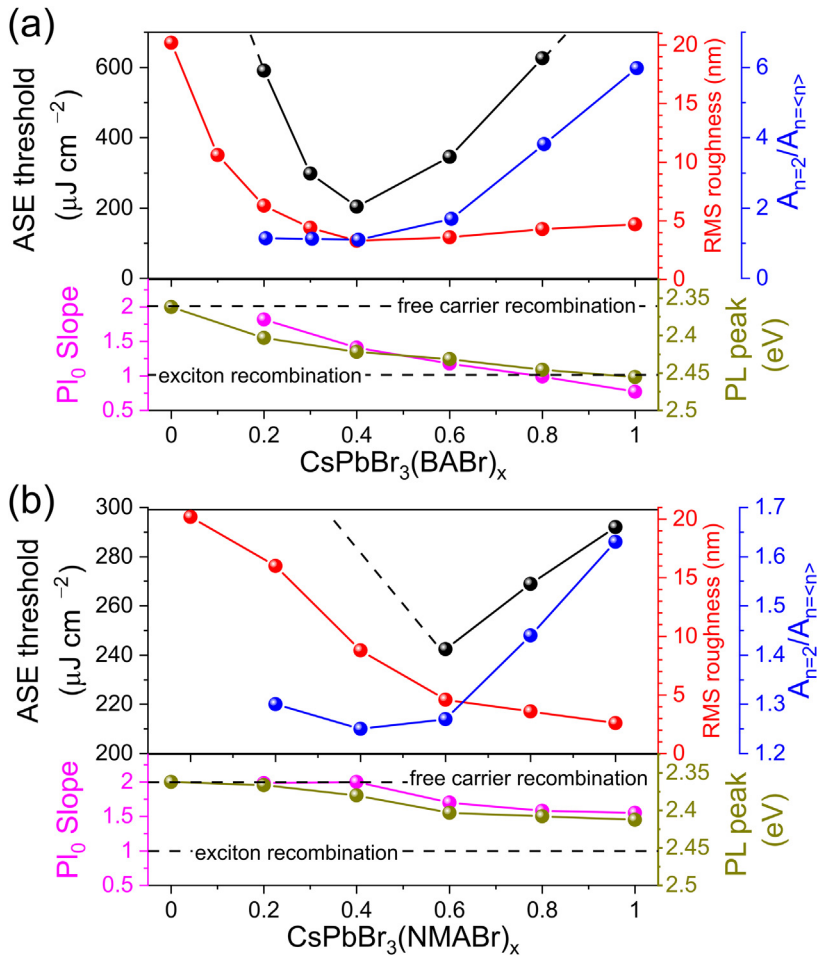

FIGURE 4

Key findings showing that a reduction in the volume fraction of the small QWs is essential for achieving good ASE thresholds of quasi-2D perovskites. The relationship among the ASE threshold, film roughness, ratio of absorbance of the $n = 2$ to large-n QWs, the power law of the PL_0 slope, and the PL peak energy (below ASE threshold) for (a) BABr and (b) NMABr based quasi-2D perovskites are presented as a function of 2D spacer concentration. $A_{n=2}$ and $A_{n=<n>}$ is the absorbance at 434 nm ($n = 2$) and 500 nm ($n = <n>$). PL_0 slope is the slope of the linear fit of plots of PL_0 versus the pump energy densities on a log–log scale. The dotted lines indicate the PL_0 slope and the emission energy expected for pure free carrier recombination and pure exciton recombination. Note that the slope of 0.77 (<1) for $BA_{1.0}$ sample can be attributed to the faster EEA process induced the underestimate of PL_0 (see Supplementary Note 2).

whereas for pure excitonic emission (as in the $BA_{0.8}$ quasi-2D material) the emission peak is at 2.45 eV. For both the BA and NMA linkers, when the 2D-spacer concentration is reduced the PL_0 slope metric and peak position metric both move toward a greater contribution from free carrier recombination. Furthermore, even at high 2D-spacer concentrations the NMA films always show a significant contribution from free carrier recombination to their emission. This is consistent with the NMA films also showing a much smaller volume fraction of small QWs, even at high 2D-spacer concentrations.

To summarize, it is critical to reduce the roughness and to shift the emission mechanism from purely excitonic towards free-carrier recombination to improve ASE performance in quasi-2D perovskites. Reducing the volume fraction of small n QWs can be achieved by the type of 2D spacer used (i.e., NMA rather than BA) and its molar ratio with respect to the monovalent cation. The reduction in the volume fraction of small-n QWs causes a greater contribution of free-carrier recombination to the emission mechanism and also lowers the ASE threshold. At small concentrations of the NMA linker, the recombination mechanism indeed seems to be purely free carrier based (as in the 3D films). Although the film roughness of these NMA films with low 2D-linker concentration is too rough as processed to achieve ASE, we do note that after low-temperature imprinting step (65 °C, 600 bar, 10 min, Fig. S24) that the roughness in these films can be reduced to 1.0 nm and an ASE threshold of 200 μJ/cm^2 achieved.

ASE in 3D materials: HTA of quasi-2D films versus standard routes

In the previous sections, we demonstrated that the two primary factors for improving ASE performance in quasi films were: (1) an emission mechanism based on bimolecular recombination (which could be achieved by control of the QW thickness distribution), and (2) smooth films. In this section, we demonstrate that the 3D material created by HTA of a quasi-2D film can achieve the same ASE threshold as 3D films created by thermal imprinting a directly formed 3D layer. This is the case even

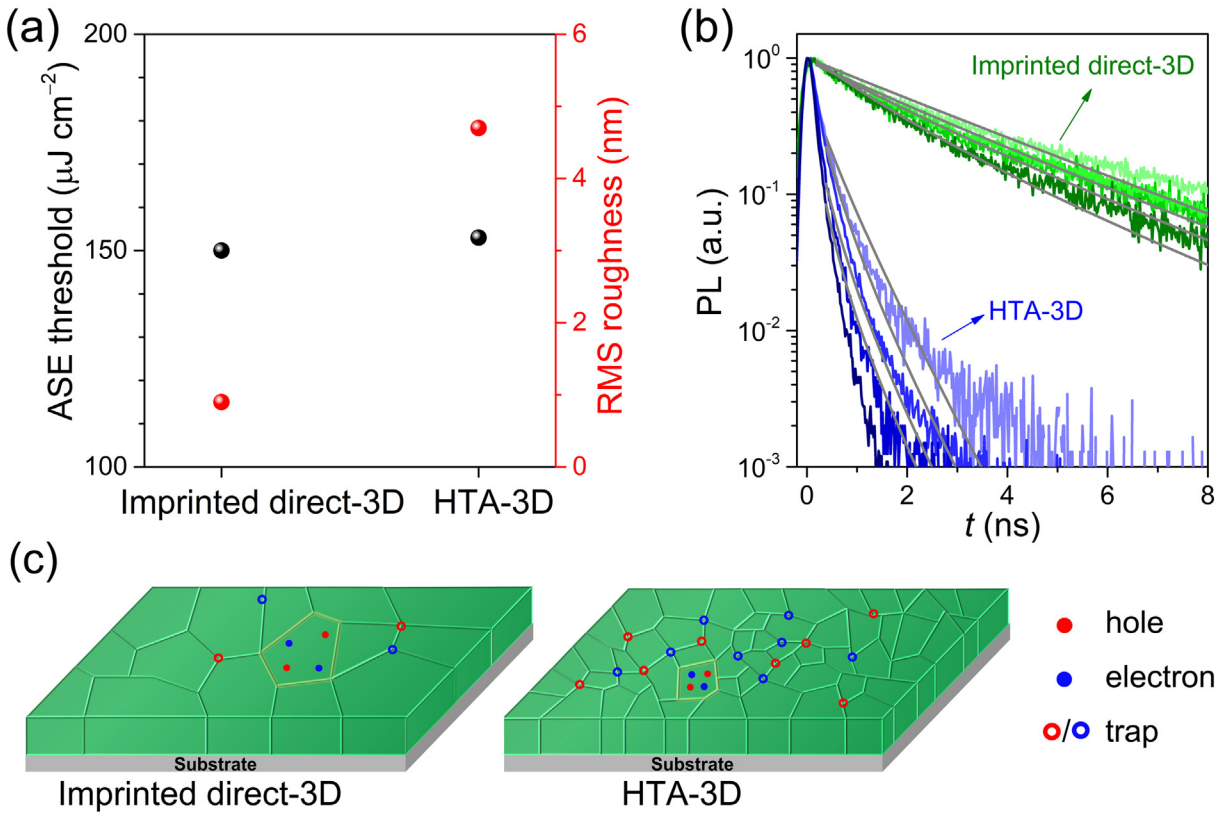

FIGURE 5

Comparison of ASE and carrier dynamics between 3D films processed by a conventional route (thermal imprinting of spin-coat 3D film) versus HTA of a quasi-2D film. (a) ASE thresholds and RMS surface roughness of the films (full data in Fig. S25). (b) Normalized TRPL decays of imprinted direct-3D and HTA-3D recorded with a streak camera setup following the excitation at 343 nm (1 kHz, 260 fs) with excitation fluences varying from 1 μJ cm^{-2} to 8 uJ cm^{-2}. The fluences are sufficiently low such that ASE does not affect the dynamics and the gray solid lines are the fits to extract the trap-assisted and bimolecular recombination rates according to the rate equation model described in the text. (c) Schematic illustration of the difference between imprinted direct-3D and HTA-3D films in crystal size, confinement of free charge carriers and trap densities.

though the latter layer is smoother. In agreement with our observations for the quasi-2D materials, these results stress the importance of low scattering and a fast rate of emission for reaching the high densities of wave-guided photons in the perovskite film necessary for low ASE thresholds.

The 3D films formed directly by spin coating have too rough surfaces to show ASE, as previously discussed. To improve the ASE performance of the directly formed 3D film, we again carried out thermal imprinting with a flat stamp (150 °C, 900 bar, 10 min). Fig. 5a demonstrates the 22 nm RMS roughness is reduced after imprinting to 0.9 nm, and an ASE threshold after imprinting of 150 μJ cm^{-2} (see Fig. S25 for data). Thermal imprinting has also been found to recrystallize the perovskite leading to larger grains, and an enhancement of the PLQY (especially at low charge carrier densities) due to reduction in the trap-assisted recombination rate (k_1 in Eqn. (3)) [45,46]. As illustrated in Fig. S26, we observe the PL lifetime of the direct-3D film is minorly extended after imprinting, and the fluence dependent data confirm that this is due to a reduction in k_1. The XRD peaks also narrow after thermal imprinting (Fig. S27). Roughly estimating the ordered crystallite size from the peak width of the XRD diffractogram leads to estimates of 54 and 59 nm before and after thermal imprinting respectively.

The characteristics of the 3D film created by HTA of a quasi-2D film ($BA_{0.4}$) are also presented in Fig. 5a with data shown in Fig. S25. Although the 4.7 nm roughness of the HTA 3D film is higher than imprinted direct-3D film the threshold is the same (153 μJ cm^{-2} vs. 150 μJ cm^{-2}). The XRD peaks (Fig. S27) are also significantly broader, leading to an estimate of the ordered crystallite size of 32 nm.

The ASE threshold depends on the product of the waveguided photon density and the excited-state density. The rate of photon loss is likely higher in the HTA film due to its worse roughness (see supplementary note 4). However, the reduction in photon density caused by an increased rate of scattering loss could be compensated by a faster rate of bimolecular recombination. The PL transients for a sequence of excitation fluences for both films in Fig. 5b examine this possibility. Qualitatively, the decay in the HTA film is always much faster indicating a higher k_1. This is consistent with faster arrival of carriers at grain boundary trapping sites in the smaller grains in the HTA film. Nonetheless, significant differences in the rate of photon emission are apparent for the different fluences indicating that bimolecular recombination can still effectively compete with the fast carrier trapping in the HTA-3D films. For the direct imprinted 3D film, although k_1 is slower, so too must be k_2, because if k_2 were the same as in the

TABLE 2

Rate coefficients obtained from global fitting the TRPL decays of different 3D films.

	k_1 (s^{-1})	k_2 (cm^3 s^{-1})
Imprinted direct-3D	$(1.52 \pm 0.22) \times 10^8$	$(2.11 \pm 0.10) \times 10^{-10}$
HTA-3D	$(7.90 \pm 1.54) \times 10^8$	$(5.00 \pm 0.87) \times 10^{-9}$
HTA-3D/PMMA	$(2.00 \pm 0.23) \times 10^8$	$(3.12 \pm 0.14) \times 10^{-9}$

HTA film the TRPL decay for the imprinted film would become dominated by k_2 at higher fluences and reach sigillary short lifetimes to the HTA film.

A simple quantitative analysis of the TRPL data supports the conclusion of an enhanced k_2 in the smaller grains of the HTA 3D sample. Given the PL is due to bimolecular carrier recombination it is related to the photoexcited carrier density by:

$$PL(t) \propto n(t)^2 \quad (4)$$

where $n(t)$ is the carrier density at time delay t, which can be obtained from an analytical solution of Eqn. (3) (neglecting Auger processes as they are insignificant in this fluence range). Globally fitting the TRPL transients for a given sample (sharing k_1 and k_2) allows the trapping and bimolecular recombination rate to be estimated for the HTA and imprinted films. The extracted rates are summarized in Table 2. The value for k_1 found for the imprinted 3D film gives a time constant of 7 ns, which is in reasonable agreement with the 19 ns lifetime reported in the literature [45] for recrystallized $CsPbBr_3$. Similarly, the value found for bimolecular recombination of $(2.11 \pm 0.10) \times 10^{-10}$ cm^3 s^{-1} is in good agreement with values found in directly formed 3D films of $CH_3NH_3PbI_3$ (and similar films with mixed cations) [47,48]. The increase in k_1 in the HTA is consistent with the increased density of traps in the smaller grains of this film (as schematically illustrated in Fig. 5c) [49]. The increase in k_2 for the HTA film with decreased grain size is also consistent with recent observations in CH_3NH_3PbI, wherein k_2 increased from 1×10^{-10} cm^3 s^{-1} to 2×10^{-9} cm^3 s^{-1} when the grain size of the film was changed from 170 to 30 nm [47]. Such an increase in k_2 may be understood in terms of an increased encounter rate of electron-hole pairs created in the same grain. Reflection of the charge carriers at the grain boundary could somewhat restrict the diffusion of the charge carriers, enhancing their probability for encountering one another. We also note it has been shown that bimolecular recombination is an inverse absorption processes, and that the Coulomb enhancement of the free carrier absorption leads to an enhancement also of k_2 [50]. Increase of the exciton binding energy increases the Coulomb enhancement of the free carrier absorption, and therefore tuning of k_2 in QW structures via careful selection of the exciton binding energy could be possible. For example, an increase of k_2 from 1×10^{-10} cm^3 s^{-1} to 10×10^{-10} cm^3 s^{-1} with decreasing $CsPbBr_3$ nanocrystal size (from 10 to 6 nm) has been observed [51].

In summary, we find that HTA of quasi-2D films leads to 3D films with ASE thresholds comparable to those obtained by the more rigorous route of thermally imprinting directly created 3D films. The similar ASE threshold despite the worse surface roughness of the HTA-3D film suggest that the rate of emission may be faster in the HTA-3D film, a suggestion that is supported by comparison of the fluence-dependent TRPL data for the two films.

As a further note, we confirm that the fast k_1 rate in the HTA 3D film does not compromise the ASE performance. To reduce k_1, we used the passivation strategy of depositing a thin layer of PMMA on top of HTA-3D film. As shown in Fig. S28a, compared to the pristine HTA film the PMMA capped film is obviously brighter under a UV lamp, and the fluence-dependent TRPL measurements indeed indicate a reduced k_1. Global fitting the TRPLs (Table 2) revealed the first order rate constant of PMMA capped film is almost one quarter of that of the pristine HTA-3D film, and similar to that of the imprinted 3D film. Supporting, our previous analysis, the k_2 is not significantly affected by the addition of PMMA and remains much faster than in the imprinted direct 3D film. The ASE threshold (Fig. S28b-d) of pristine and PMMA capped HTA-3D films are comparable, confirming that first order rate has a negligible effect on the ASE threshold because the rate of bimolecular recombination greatly exceeds k_1 in both cases at the early times after excitation (during which ASE occurs). These results further support our conclusions that optimizing bimolecular recombination and reducing the rate of photon loss due to scattering are the essential parameters to control to further develop perovskite gain materials.

Discussion

To improve the ASE and lasing performance of quasi-2D perovskites, the exciton annihilation processes need to be carefully considered (such as the EEA demonstrated here, but also exciton charge annihilation in the case of electrical pumping). To slow down the EEA process, increasing the volume fraction of thick QWs in quasi-2D perovskite can be achieved by controlling the 2D spacer (i.e., utilizing NMA instead of BA), and by reducing the 2D spacer concentration. The shift to lower volume fractions of low-n, thin, QWs correlates with a shift towards free carrier emission. Efforts towards optimizing the film fabrication process (i.e., solvent engineering, additive engineering) to achieve smooth films at low spacer content are critical. One promising route to planarize quasi-2D films of moderate roughness is imprinting [34]. Finally, materials strategies to engineer the free carrier recombination rate are of interest. In this regard, the control of the QW thickness and lateral area are key, as the constraint of carrier pairs to a controlled volume should manipulate their encounter rate, and thereby provide a mechanism for engineering the recombination rate. Development of new ligands to influence the carrier distribution and mobility in QWs should also be considered.

Our conclusion that the ASE thresholds (measured under pulsed conditions) for quasi-2D materials tend to be higher than their 3D counterparts appear surprising considering the recent major success communicated by Qin and coworkers achieving CW room-temperature lasing based on quasi-2D materials [15]. However, our conclusions are not as contradictory as they may first appear. Firstly, our results indicate that the increase in the ASE threshold of the quasi-2D material decreases as the molar ratio of the 2D spacer to the $CsPbBr_3$ precursor decreases. By a spacer ratio of 0.4, the quasi-2D material had a threshold within

a factor of 2 of its 3D counterparts and using the NMA ligand in low concentrations lead to emission that was completely dominated by free carrier recombination. The work by Qin and coworkers used a molar ratio of 0.25 2D spacer to the $FAPbBr_3$ cursor and achieved excellent quality quasi-2D perovskite films of $\langle n \rangle$=8 [15]. Examining their absorption spectra, the high-energy excitonic peaks from low n QWs are not pronounced, indicating that a large volume fraction of their film is composed of higher n QWs. These observations are therefore consistent with our conclusion that correctly adjusting (maximizing) the volume fraction of large-n QWs in the quasi-2D material is critical for stimulated emission applications. Furthermore, Qin and coworkers suggest in their recent achievement of room temperature CW lasing in quasi-2D perovskites [15] that triplet excitons impede the population inversion due to their inability to participate in gain, but the ability to participate in annihilation, suggesting that they also may be involved in lasing death under CW pumping. A detailed comparison of the mechanisms of lasing death under long-pulse (quasi-CW) may also reveal advantages of the quasi-2D versus the 3D material that contribute to the success of the former. We recorded the TRPL of our $CsPbBr_3(BABr)_{0.8}$ thin film under vacuum and in air (triplet quencher), and an increase in delayed PL component from air to vacuum could be observed (Fig. S29a). However, the ASE spectra acquired under vacuum and air generated the comparable ASE thresholds (Fig. S29b-d), which are expected to be lower in air case due to the reduced singlet–triplet exciton annihilation rate by quenching of the triplet excitons. Further careful examination of whether and how the spin-state of the exciton plays a role in the excited-state dynamics of these quasi-2D materials is of ongoing interest, but our results suggest that it may rather be the optimization of bimolecular recombination of free carriers in quasi-2D materials that is the key to their success as gain materials.

Conclusion

To summarize, we investigated the spontaneous emission (PL) and ASE properties of a series of quasi-2D perovskites and their 3D counterparts. The experimental results show that the superior PL characteristic of quasi-2D perovskites based on BA spacers at low excitation fluence does not translate into lower ASE thresholds. Surprisingly, annealing the quasi-2D perovskites into the 3D perovskites results in lower ASE thresholds despite the much less efficient PL of the 3D film at low excitation power densities. This can be fully explained by the differences between excitonic and free carrier emission that dominate the emission from quasi-2D and 3D perovskite, respectively. The excitonic emission of the quasi-2D materials is a linear process, whose efficiency is decreased by the nonradiative second-order process of EEA. This means that the emission efficiency (high at low excitation fluences) is drastically reduced at higher fluences. The decrease in emission efficiency with increasing excitation density significantly increases the ASE threshold of the quasi-2D materials. The free carrier emission in the 3D material is a second-order process, whose efficiency increases with excitation fluence. This allows the 3D materials to reach ASE at lower excitation fluences than the quasi-2D materials whose emission is purely excitonic. Importantly, the ASE threshold in quasi-2D materials can be optimized by shifting the emission away from exciton recombination to radiative free charge carrier recombination. By reducing the volume fraction of small n QWs through the choice of 2D spacer and its concentration, we demonstrate that the emission mechanism can be tuned towards free carrier recombination and the ASE threshold concurrently improved. The reduction in the volume fraction is achieved by reducing the concentration of the 2D-spacer, or by utilizing the spacer NMA rather than BA or PEA. These results suggest a roadmap for optimization of quasi-2D materials for gain applications wherein the volume fraction of large-n QWs should be maximized, and the rate of free carrier recombination in these larger QWs be made as efficient as possible. Further development of control methods for QW thickness and size, including the development of new ligands is of central importance in this respect.

Finally, we also demonstrate that 3D film created by annealing of a quasi-2D film had much better surface morphology (and therefore much lower ASE thresholds) than directly created neat 3D film. Even after the directly created 3D film is thermally imprinted to reduce its surface roughness below that of the 3D film created by HTA of a quasi-2D film, the HTA-3D film still has a similar ASE threshold to the imprinted film. In addition to the promising routes for development suggested above, quasi-2D films should be considered as precursors for 3D films. The favorable ASE thresholds in HTA-3D films suggest that surface and grain size control of 3D $CsPbBr_3$ films through HTA of quasi-2D films is a promising strategy for creating thin perovskite films for gain applications. Our results highlight that further efforts to understand and increase the rate of bimolecular recombination in perovskites are of central interest for light-emitting applications.

Experimental section

Materials

$CsPbBr_3$ (>98.0%) was purchased from TCI. *n*-Butylammonium bromide (BABr, 98%), 2-phenethylammonium bromide (PEABr, >98%) and DMSO (>99.0%) were purchased from Sigma Aldrich. 1-Naphthylmethylamine Bromide (NMABr, >99%) and TPBi (>99.5%) were purchased from Lumtec. 12-Crown-4 (>98%) and LiF were purchased from Alfa Aesar. PEDOT:PSS (Clevios PV, AI 4083) was purchased from Heraeus. All chemicals were used without further purification.

Perovskite film fabrication

239.1 mg $CsPbBr_3$ and 5.3 mg 12-Crown-4 were first dissolved into 1 ml DMSO, followed by heating at 60 °C for ~ 20 min. BABr/DMSO (2.8 M) stock solution was then added into above solution to make the perovskite precursor solution with a stoichiometry of $CsPbBr_3(BABr)_x$. The perovskite precursor solution was then spin-coated onto the substrates with a consecutive two-step process: 1000 rpm for 20 s (ramp rate 1000 rpm s^{-1}) and 4000 rpm for 40 s (ramp rate 1000 rpm s^{-1}). Subsequently, the film was annealed at the specific temperature for 10 min: 70 °C for all quasi-2D films, 150 °C for BABr based 3D films, and 250 °C for PEABr and NMABr based 3D films. 12-Crown-4 was employed as the additive for all the perovskite films to improve the film quality and inhibit the crystallization of 2D spacer [7].

Characterization

ASE measurement

For nanosecond threshold measurements, a diode-pumped passively Q-switched solid-state laser (CryLaS, FTSS355-Q2) was used as the excitation source (355 nm, <1.1 ns, 1 kHz) with the spot size of 1.78×10^{-3} cm^2. Pump intensities were tuned through changing the position of the variable neutral density filter, and the corresponding PL spectra were collected with an Ocean Optics spectrometer (USB 2000+). Measurements were conducted in a nitrogen-filled glovebox. For the ASE measurement shown in Figs. S5 and S29, a femtosecond amplifier with optical parametric amplifier for frequency conversion was used (Light Conversion, Pharos/Orpheus). The excitation was 405 nm, 260 fs, and 1 kHz. An Avantes spectrometer (AvaSpec-2048L) was used to collect the emission, and the measurements were conducted under vacuum condition. Spot size of the fs laser was 7.80×10^{-3} cm^2, acquired with a laser beam profiler (Thorlabs). All the samples were deposited on the glass substrate for ASE measurements.

UV–vis absorption spectra

Absorption spectra of perovskite films were collected using a Lambda 1050 UV/Vis/NIR Spectrophotometer (PerkinElmer) equipped with an integrating sphere.

PLQY measurements

PLQY of the perovskite films were conducted on a home-made setup, equipped with a CW laser diode (Thorlabs), an integrating sphere, an optical fiber, and a spectrometer (Avantes-2048L). The samples were excited at 405 nm, and the PLQY were obtained based on the standard 3 step method. Pump power was scanning from 5 μW to 40 mW through changing the position of the neutral-density filter. To obtain a wide range of pump power density, the PLQY under unfocused (spot size, 4.12×10^{-2} cm^2) and focused (spot size, 8.82×10^{-4} cm^2) laser beam was both recorded. The L_{in}-L_{out} curves (CW excitation) shown in Figs. S4b, S16, S19 and S22 are all acquired using the same setup.

AFM images

Topographic images of perovskite films on glass substrates were obtained by atomic force microscopy using Nano Wizard II (JPK Instruments). The RMS (Root-Mean-Square) roughness is calculated using the free software (Gwyddion).

TRPL measurements

The TRPLs were recorded by a streak camera (Hamamatsu Universal C10910) equipped with a spectrometer (Acton SpectraPro SP2300), and the third harmonic of the amplifier (Light Conversion, Pharos/Hiro, 260 fs, 1030 nm, 1 kHz) were adopted as the excitation laser. To acquire the PL_0, the MCP gain and exposures of streak camera were kept the same for all the pump power densities, and ND filters were used to avoid the overexposure of the camera. PL_0 were calculated through integrating the PL spectra of time zero, and the PL intensities were also corrected for the appropriate ND filter.

TA measurement

TA measurement was performed with a custom-built setup. The femtosecond laser beam was generated from PHAROS (Light conversion, 260 fs, 1030 nm, 2 kHz), then split into two parts by a 3/1 beam splitter: the minor portion of the laser beam was focused onto a sapphire crystal to produce the probe beam of white light continuum; the major portion was delivered into an optical parametric amplifier (Orpheus, Light conversion) for the generation of pump beam with a specific wavelength. The pump beam successively passed through a chopper (1 kHz) and an optical delay line, and finally focused onto the sample, spatially coincide with the probe beam. To ensure all the excited area was probed, the probe beam size is set a little bit larger than that of pump beam. Each pulse of the probe spectrum was read out into a LabView program and adjacent spectra were used to calculate the transient absorption signal (ΔA). The perovskite samples were deposited on the glass substrate and pumped at 405 nm. To minimize the effect of ASE, the fs-TA spectra were only collected at the power below ASE threshold.

Nanoimprint end-of-line. The instrument and imprinting process details can be found in our previous study [36] and the imprinting parameters used in this work are 65 °C, 600 bar, 10 min and 150 °C, 600 bar, 10 min for quasi-2D film and 3D film respectively.

Data availability

All data required to reproduce the results in the paper are available in main text and the Supplementary Materials.

CRediT authorship contribution statement

Yang Li: Conceptualization, Software, Validation, Formal analysis, Investigation, Data curation, Writing - original draft, Visualization. **Isabel Allegro:** Investigation, Formal Analysis, Writing - review & editing. **Milian Kaiser:** Validation, Investigation, Writing - review & editing. **Aditya J. Malla:** Investigation, Writing - review & editing. **Bryce S. Richards:** Resources, Writing - review & editing, Supervision. **Uli Lemmer:** Conceptualization, Resources, Writing - review & editing, Supervision, Funding acquisition. **Ulrich W. Paetzold:** Conceptualization, Resources, Data curation, Writing - original draft, Writing - review & editing, Supervision, Funding acquisition. **Ian A. Howard:** Conceptualization, Methodology, Formal analysis, Resources, Data curation, Writing - original draft, Writing - review & editing, Supervision, Funding acquisition.

Declaration of Competing Interest

The authors declare that they have no known competing financial interests or personal relationships that could have appeared to influence the work reported in this paper.

Acknowledgements

The authors gratefully acknowledge funding from the DFG (PEROLAS, No. 409035484), the Karlsruhe School of Optics & Photonics (KSOP), the Helmholtz Energy Materials Foundry (HEMF), and the Excellence Cluster "3D Matter Made to Order" (3DMM2O). Authors are grateful to Karlsruhe Nano Micro Facility (KNMF) at IMT/KIT for the help on nanoimprint process.

Appendix A. Supplementary data

Supplementary data to this article can be found online at https://doi.org/10.1016/j.mattod.2021.05.002.

References

[1] L.N. Quan et al., Chem. Rev. 119 (2019) 7444–7477. https://pubs.acs.org/doi/10.1021/acs.chemrev.9b00107.

[2] J. Byun et al., Adv. Mater. 28 (2016) 7515–7520, https://doi.org/10.1002/adma.201601369.

[3] M. Yuan et al., Nat. Nanotech. 11 (2016) 872–877. https://www.nature.com/articles/nnano.2016.110.

[4] N. Wang et al., Nat. Photon. 10 (2016) 699–704. https://www.nature.com/articles/nphoton.2016.185.

[5] X. Yang et al., Nat. Commun. 9 (2018) 570. https://www.nature.com/articles/s41467-018-02978-7.

[6] B. Zhao et al., Nat. Photon. 12 (2018) 783–789. https://www.nature.com/articles/s41566-018-0283-4.

[7] M. Ban et al., Nat. Commun. 9 (2018) 3892. https://www.nature.com/articles/s41467-018-06425-5.

[8] Y. Shang et al., Sci. Adv. 5 (2019) eaaw8072. https://advances.sciencemag.org/content/5/8/eaaw8072.

[9] H. Zhang et al., Adv. Mater. 30 (2018) 1706186. https://onlinelibrary.wiley.com/doi/full/10.1002/adma.201706186.

[10] M.R. Leyden et al., Phys. Chem. Chem. Phys. 20 (2018) 15030–15036. https://pubs.rsc.org/en/content/articlelanding/2018/cp/c8cp02133c#!divAbstract.

[11] C.M. Raghavan et al., Nano Lett. 18 (2018) 3221–3228, https://doi.org/10.1021/acs.nanolett.8b00990.

[12] Y. Liang et al., Adv. Mater. 31 (39) (2019) 1903030, https://doi.org/10.1002/adma.201903030.

[13] M.R. Leyden et al., ACS Photonics 6 (2019) 460–466. https://pubs.acs.org/doi/10.1021/acsphotonics.8b01413.

[14] L. Lei et al., Adv. Mater. 32 (2020) 1906571. https://onlinelibrary.wiley.com/doi/full/10.1002/adma.201906571.

[15] C. Qin et al., Nature 585 (2020) 53–57. https://www.nature.com/articles/s41586-020-2621-1.

[16] H. Kim et al., Nat. Commun. 9 (2018) 4893. https://www.nature.com/articles/s41467-018-07383-8.

[17] H. Kim et al., Adv. Optical Mater. 8 (2020) 1901297. https://onlinelibrary.wiley.com/doi/full/10.1002/adom.201901297.

[18] C. Zou et al., ACS Nano 14 (2020) 6076–6086. https://pubs.acs.org/doi/10.1021/acsnano.0c01817.

[19] J.-C. Blancon et al., Nat. Commun. 9 (2018) 2254. https://www.nature.com/articles/s41467-018-04659-x.

[20] C.C. Stoumpos et al., Chem. Mater. 28 (2016) 2852–2867. https://pubs.acs.org/doi/10.1021/acs.chemmater.6b00847.

[21] L. Mao, C.C. Stoumpos, M.G. Kanatzidis, J. Am. Chem. Soc. 141 (2019) 1171–1190. https://pubs.acs.org/doi/10.1021/jacs.8b10851.

[22] G. Xing et al., Nat. Commun. 8 (2017) 14558. https://www.nature.com/articles/ncomms14558.

[23] M. Li et al., Adv. Funct. Mater. 28 (2018) 1707006. https://onlinelibrary.wiley.com/doi/abs/10.1002/adfm.201707006.

[24] G. Delport et al., J. Phys. Chem. Lett. 10 (2019) 5153–5159. https://pubs.acs.org/doi/abs/10.1021/acs.jpclett.9b01595.

[25] S. Deng et al., Nat. Commun. 11 (2020) 664. https://www.nature.com/articles/s41467-020-14403-z.

[26] M. Gramlich et al., J. Phys. Chem. Lett. 11 (2020) 5361–5366. https://pubs.acs.org/doi/abs/10.1021/acs.jpclett.0c01291.

[27] M. Cui et al., J. Phys. Chem. Lett. 11 (2020) 5734–5740. https://pubs.acs.org/doi/abs/10.1021/acs.jpclett.0c01852.

[28] C. Qin et al., Nat. Photon. 14 (2020) 70–75. https://www.nature.com/articles/s41566-019-0545-9.

[29] H. Chen et al., Sci. Adv. 6 (2020) eaay4045. https://advances.sciencemag.org/content/6/4/eaay4045.

[30] Z. Li et al., Nat. Commun. 10 (2019) 1027, https://doi.org/10.1038/s41467-019-09011-5.

[31] Y.F. Ng et al., Chem. Mater. 32 (2020) 8097–8105, https://doi.org/10.1021/acs.chemmater.0c00513.

[32] S. Yakunin et al., Nat. Commun. 6 (2015) 8056. https://www.nature.com/articles/ncomms9056.

[33] F. Yuan et al., J. Phys. Chem. C 121 (2017) 15318–15325. https://pubs.acs.org/doi/abs/10.1021/acs.jpcc.7b02101.

[34] Y. Jia et al., Adv. Optical Mater. 8 (2019) 1901514. https://onlinelibrary.wiley.com/doi/full/10.1002/adom.201901514.

[35] N. Pourdavoud et al., Adv. Mater. 29 (2017) 1605003. https://onlinelibrary.wiley.com/doi/full/10.1002/adma.201605003.

[36] P. Brenner et al., Nat. Commun. 10 (2019) 988. https://www.nature.com/articles/s41467-019-08929-0.

[37] C. Changsoon et al., ACS Appl. Mater. Interfaces 12 (2020) 35242–35249. https://pubs.acs.org/doi/10.1021/acsami.0c08870.

[38] J.M. Richter et al., Nat. Commun. 7 (2016) 13941. https://www.nature.com/articles/ncomms13941.

[39] M.B. Johnston, L.M. Herz, Acc. Chem. Res. 49 (2016) 146–154. https://pubs.acs.org/doi/10.1021/acs.accounts.5b00411.

[40] S. Zhang et al., Photon. Res. 8 (2020) A72–A90. http://www.osapublishing.org/prj/abstract.cfm?URI=prj-8-11-A72.

[41] W. Zhai et al., Appl. Phys. Lett. 114 (2019). https://aip.scitation.org/doi/abs/10.1063/1.5090569 131107.

[42] P.K. Roy et al., Nanoscale 12 (2020) 18269–18277, https://doi.org/10.1039/D0NR01171A.

[43] L. Lei et al., Adv. Funct. Mater. (2021) 2010144. https://onlinelibrary.wiley.com/doi/abs/10.1002/adfm.202010144.

[44] K. Zheng et al., J. Phys. Chem. C 120 (2016) 3077–3084. https://pubs.acs.org/doi/full/10.1021/acs.jpcc.6b00612.

[45] N. Pourdavoud et al., Adv. Mater. 31 (39) (2019) 1903717, https://doi.org/10.1002/adma.201903717.

[46] R. Schmager et al., Adv. Funct. Mater. 30 (9) (2020) 1907481, https://doi.org/10.1002/adfm.201907481.

[47] Z. Chen et al., Adv. Mater. 30 (2018) 1801370. https://onlinelibrary.wiley.com/doi/abs/10.1002/adma.201801370.

[48] I. Allegro et al., J. Phys. Chem. Lett. 12 (9) (2021) 2293–2298, https://doi.org/10.1021/acs.jpclett.1c00099.

[49] Q. An, et al., Matter. https://doi.org/10.1016/j.matt.2021.02.020.

[50] C.L. Davies et al., Nat. Commun. 9 (2018) 293, https://doi.org/10.1038/s41467-017-02670-2.

[51] S.G. Motti et al., Adv. Funct. Mater. 30 (2020) 1909904, https://doi.org/10.1002/adfm.201909904.